



Diagnosing and correcting anode-free cell failure via electrolyte and morphological analysis

A. J. Louli¹, A. Eldesoky², Rochelle Weber^{3,4}, M. Genovese¹, Matt Coon¹, Jack deGooyer¹, Zhe Deng⁵, R. T. White⁶, Jaehan Lee⁶, Thomas Rodgers⁶, R. Petibon⁴, S. Hy⁴, Shawn J. H. Cheng⁴ and J. R. Dahn^{1,2} ✉

Anode-free lithium metal cells store 60% more energy per volume than conventional lithium-ion cells. Such high energy density can increase the range of electric vehicles by approximately 280 km or even enable electrified urban aviation. However, these cells tend to experience rapid capacity loss and short cycle life. Furthermore, safety issues concerning metallic lithium often remain unaddressed in the literature. Recently, we demonstrated long-lifetime anode-free cells using a dual-salt carbonate electrolyte. Here we characterize the degradation of anode-free cells with this lean (2.6 g Ah⁻¹) liquid electrolyte. We observe deterioration of the pristine lithium morphology using scanning electron microscopy and X-ray tomography, and diagnose the cause as electrolyte degradation and depletion using nuclear magnetic resonance spectroscopy and ultrasonic transmission mapping. For the safety characterization tests, we measure the cell temperature during nail penetration. Finally, we use the insights gained in this work to develop an optimized electrolyte, extending the lifetime of anode-free cells to 200 cycles.

Higher-energy-density batteries will increase the range of electric vehicles, decrease their cost and even enable electrified urban aviation. To develop electric vertical take off and landing vehicles capable of urban aviation, several analyses have estimated that batteries with a specific energy density of 400 Wh kg⁻¹ at the cell level—or 30% higher than current lithium-ion (Li-ion) cells—are required^{1,2}. For land-based electric vehicles, volumetric energy density is more important. Today's electric vehicles³ can have ranges of up to 400 km; if those battery packs were made using cells with 60% higher volumetric energy density, with little cost difference per cell, then the vehicle range would be extended by an additional 280 km for the same cost (Fig. 1d). Increased volumetric energy can also impact cost—if these high-energy cells were used to build a battery pack that could sustain the same original 400 km range, many fewer cells would be required, substantially decreasing the pack cost (Fig. 1e).

Anode-free lithium metal cells deliver 60% higher energy density than that of Li-ion cells. Figure 1a shows an anode-free cell (left) next to a Li-ion cell (right). Schematics of these cell designs are shown in Fig. 1b,c with the cell parameters listed in Supplementary Table 1. Both cells utilize the same Li[Ni_{0.5}Mn_{0.3}Co_{0.2}]₂O₄ (NMC532) cathode, but instead of a graphite host, the anode-free cell stores charge as electroplated lithium metal. Anode-free cells use zero excess lithium—100% of the lithium comes from the positive electrode^{4,5}. Many lithium metal cells reported in the literature are actually less energy dense than Li-ion cells due to the substantial amount of excess lithium used^{6,7}. Supplementary Fig. 1b shows that use of lithium foil thicker than 60 μm renders lithium metal cells less energy dense than Li-ion cells. Moreover, not using lithium foil will decrease costs and increase compatibility with current cell production infrastructure⁸. Figure 1c,d shows the stack energy density and projected⁹ 18650 cell energy density of cells with a positive electrode

loading of 15.7 mg cm⁻² (3.1 mAh cm⁻²), and Supplementary Fig. 1c shows how energy density scales with increased positive electrode loading. The anode-free cells demonstrated in this work have a stack energy density of 1,200 Wh l⁻¹, 60% higher than Li-ion cells with the same positive electrode.

With zero excess lithium, anode-free cells often suffer rapid capacity loss. A cycle life of less than 20 cycles down to 80% of the original capacity is common^{5,10}. Cell failure can be attributed to lithium loss via lithium electrolyte parasitic reactions causing the formation of a solid electrolyte interphase (SEI) and electrically isolated lithium^{11–13}. Both mechanisms result in 'dead' lithium and are exacerbated by a high surface area mossy morphology which tends to form in conventional electrolytes^{11,14–16}. Electrolyte optimization^{17–19} and the application of mechanical pressure^{20–23} are among the strategies employed to increase lifetime as they promote a dense lithium morphology. Beyond cycle life, cell safety remains a challenge. Safety issues with lithium metal cells have been well-documented since the 1980s²⁴. Safety is often discussed in the literature, but is rarely tested under realistic conditions. Some reports claim to use 'non-flammable' electrolytes by virtue of the electrolyte-soaked separators not catching fire when exposed to a flame^{25,26}. However, it is insufficient to claim safety without more realistic characterization or cell abuse tests^{27,28}.

Recently, we demonstrated long-lifetime anode-free cells utilizing a dual-salt carbonate-based liquid electrolyte, sustaining 80% capacity over 90 cycles²⁹. Another more impactful metric is energy retention above Li-ion cells—that is, how long cells can deliver a greater energy density than Li-ion cells. Figure 2a shows that anode-free cells with this lean (2.2 ml Ah⁻¹ or 2.6 g Ah⁻¹) dual-salt lithium difluoro(oxalate)borate (LiDFOB) and lithium tetrafluoroborate (LiBF₄) electrolyte sustain a higher energy density than that of the optimized Li-ion cells for 120 cycles. Here we characterize

¹Department of Physics and Atmospheric Science, Dalhousie University, Halifax, Nova Scotia, Canada. ²Department of Chemistry, Dalhousie University, Halifax, Nova Scotia, Canada. ³Department of Mechanical Engineering, Dalhousie University, Halifax, Nova Scotia, Canada. ⁴Tesla Canada R&D, Dartmouth, Nova Scotia, Canada. ⁵Hua Zhong University of Science and Technology, Wuhan, China. ⁶Carl Zeiss Microscopy, Pleasanton, CA, USA.

✉e-mail: jeff.dahn@dal.ca

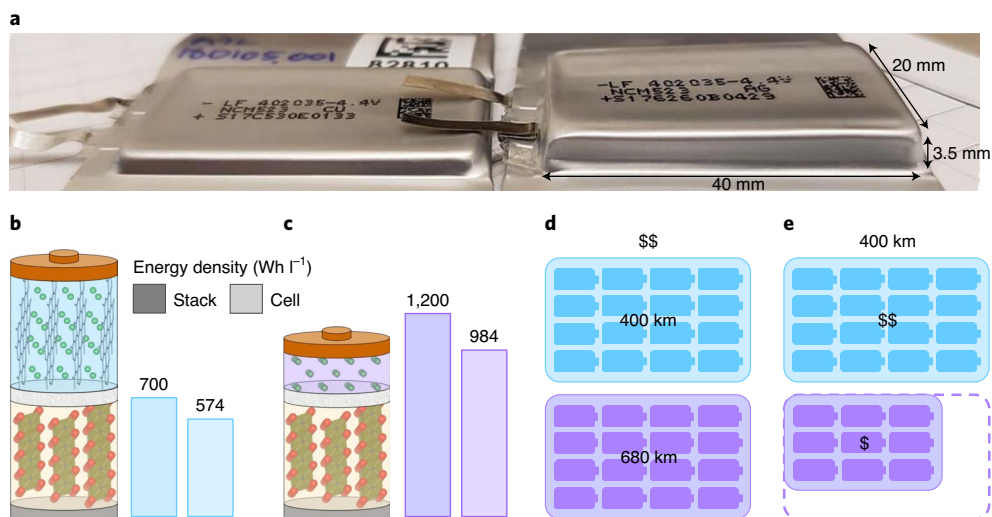


Fig. 1 | Comparison of anode-free and lithium-ion cells. **a**, Picture of an anode-free (left) and Li-ion pouch cell (right) that both have the same capacity. **b,c**, Schematic of NMC532 Li-ion (**b**) and anode-free (**c**) cells and their respective energy densities at the stack level (double-sided positive electrode, separator, double-sided negative electrode, separator), and at the cell level projected to an 18650 cell format. **d,e**, Illustration of Li-ion (top, blue) and anode-free (bottom, purple) battery packs made with the same number of cells and cost (**d**) or for the same vehicle range (**e**).

the degradation of anode-free cells with this dual-salt electrolyte. We observe the deterioration of the, initially pristine, lithium morphology using scanning electron microscopy (SEM) and X-ray tomography, and deconvolute the contribution of positive and negative electrode crosstalk towards electrolyte degradation using nuclear magnetic resonance spectroscopy (NMR). Furthermore, we observe electrolyte depletion as the lithium porosity increases using ultrasonic transmission mapping. For the safety characterization tests, we measure the cell temperature during penetration with a nail and compare this to cells using other electrolytes that are reported in the literature. Finally, we use the insights gained in this work to develop an optimized electrolyte, extending the lifetime of anode-free cells to 200 cycles.

Results

Dual-salt cell performance. Although capacity is most often reported, energy density is the most important metric for practical applications. However, most research is not performed using optimized or even similar cell formats. Therefore, comparing energy density at the cell level is difficult. Instead, stack energy density, defined as the energy contained in a sandwich of a double-sided positive electrode, separator, double-sided negative electrode and separator (depicted in Supplementary Fig. 1)—the stack that is repeated many times in an optimized cell format—is a more simple comparison to use. Furthermore, plotting energy density accounts for voltage fade and decreased reversible capacity from kinetic effects (triggered by temperature and cycling rate), which can be otherwise obfuscated in normalized capacity graphs. Figure 2a shows the stack energy density versus cycle number of anode-free cells compared to cells with an optimized Li-ion chemistry. The normalized capacity and specific energy density versus cycle are included in Supplementary Fig. 2. The anode-free cells were cycled at charge–discharge rates of C/5 and D/2, and the tests were performed at 40 °C. The anode-free cells with conventional electrolytes cannot sustain an energy density greater than Li-ion cells ($>700 \text{ Wh l}^{-1}$) for more than 20 cycles. Cells with a dual-salt 0.6 M LiDFOB and 0.6 M LiBF₄ (fluoroethylene carbonate (FEC):diethyl carbonate (DEC), 1:2 v:v) electrolyte sustain a higher energy density than that of the Li-ion cells for 100 and 120 cycles under low (170 kPa) and high (1,170 kPa) pressure, respectively. Supplementary Figs. 3 and 4 show how pressure is applied

to pouch cells in this work and further demonstrate the impact of varying the applied mechanical pressure. This long cycle life is possible because of the highly favourable dense lithium morphology enabled by the dual-salt electrolyte. However, as these cells age, the plated lithium morphology deteriorates (Fig. 2b–i). As the cells lose capacity throughout the 80 cycles, the morphology becomes less compact with a higher amount of surface area features. The worsening microscale morphology is reflected in the optical pictures of the plated lithium, shown in the insets of Fig. 2b–i, where pristine lithium appears silver and porous and dead lithium appears black¹⁵.

Electrochemical and electrolyte analysis. Figure 3a,b shows the Coulombic efficiency (CE) and zeroed charge endpoint capacity of the dual-salt cells cycled to upper cut-off voltages (UCV) of 4.3 and 4.5 V. For both UCVs, the CE declines linearly before beginning to drop off more rapidly. This drop-off occurs after 70 cycles for cells cycled to 4.5 V and after 80 cycles for cells cycled to 4.3 V. The charge endpoint capacity increases for both UCVs indicating electrolyte oxidation³⁰, with a more notable increase at the 4.5 V UCV. Interestingly, for both UCVs, the charge endpoint capacity increase slows at around the same time the CE drops off. Figure 3c shows the contributions to impedance in cells cycled to 4.5 V measured using a frequency response analyser system that measures impedance in situ³¹. The Nyquist curves for the frequency response analyser data are shown in Supplementary Fig. 5a. The charge transfer resistance (R_{ct}) was determined using the diameter of the Nyquist curve and the solution resistance (R_e) was determined using the shift of the Nyquist curve from zero³². Over the first 50 cycles, R_{ct} is stable while R_e steadily increases, as shown in the inset of Fig. 3c. After 50 cycles, both R_{ct} and R_e begin to increase more rapidly. Ex situ impedance measurements of symmetric cells taken using electrodes from cycled full cells indicate that the increase in R_{ct} is initially dominated by the positive electrode, until higher cycle counts, when the R_{ct} of the lithium electrode increases (Supplementary Fig. 5b–d). To further investigate these electrochemical trends, electrolyte degradation analysis was performed.

After cycling, the cells were taken apart for electrolyte extraction and ¹H and ¹⁹F liquid NMR was used to determine the salt and solvent changes. Figure 3d shows the molarity versus cycle number of the dual-salt cells cycled to 4.3 and 4.5 V. Initially, these cells were

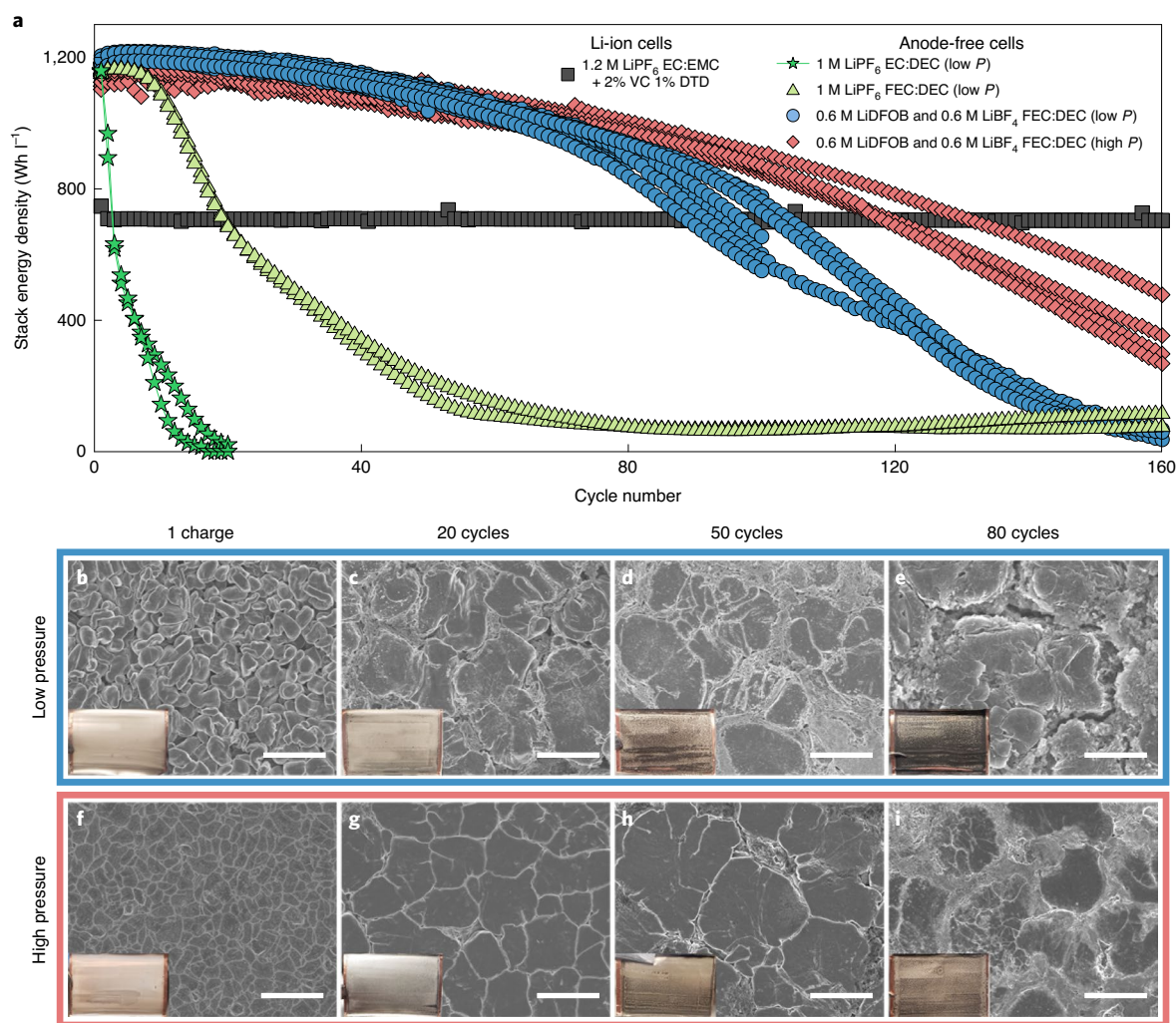


Fig. 2 | Energy retention and lithium morphology. **a**, Stack energy density versus cycle for anode-free cells with different electrolytes compared with cells with an optimized Li-ion chemistry. **b–i**, SEM images of plated lithium under low pressure ('low P ', 170 kPa, **b–e**) and under high pressure ('high P ', 1,170 kPa, **f–i**) after 1 charge (**b,f**), and 20 (**c,g**), 50 (**d,h**) and 80 (**e,i**) cycles. The insets are optical images of lithium plated on a single electrode layer collected from the pouch cell. The SEM and optical images were taken at the top of charge (4.5 V). The cells were cycled at C/5 and D/2 current rates between 3.6 and 4.5 V at 40 °C. Scale bars, 25 μm . DTD, ethylene sulfate; EC, ethylene carbonate; EMC, ethyl methyl carbonate; VC, vinylene carbonate.

filled with 0.6 M LiDFOB and 0.6 M LiBF₄ in a FEC:DEC ratio of 1:2 v:v. Both LiBF₄ and LiDFOB are consumed during cycling; however, LiBF₄ is consumed at a lower rate, seemingly independent of UCV. LiDFOB is consumed at a higher rate for cells cycled at 4.5 V compared to those cycled at 4.3 V. After ~0.3 M of LiDFOB is consumed, the consumption rate slows down for both UCVs. Thus, the increase of solution resistance (R_s) observed in Fig. 3c can be partly attributed to this continuous salt consumption causing a decrease in the ionic conductivity of the electrolyte. The greater charge endpoint capacity slippage of the cells cycled to 4.5 V observed in Fig. 3b is consistent with the higher rate of LiDFOB consumption. Moreover, the CE drop-off after ~70 cycles is concurrent with the saturation of charge endpoint capacity slippage growth and the reduced rate of LiDFOB consumption. This suggests that the reactions involving the consumption of LiDFOB are beneficial for lithium plating efficiency; when these reactions cease, the lithium morphology becomes uncontrolled and precipitates large charge transfer impedance and lithium loss resulting in cell death.

The electrolyte of the cycled symmetric cells was investigated to deconvolute the contributions of the positive and negative electrodes and crosstalk between them. Figure 3e,f shows the electrolyte

degradation data for negative and positive symmetric cells with the dual-salt electrolyte. The electrochemical cycling data for these symmetric cells are shown in Supplementary Fig. 6. Both LiBF₄ and LiDFOB are consumed in negative symmetric cells (Fig. 3e), which supports the hypothesis that this consumption is beneficial for reversible lithium plating. In positive symmetric cells, LiDFOB is consumed while an approximately equal amount of LiBF₄ is produced (Fig. 3f). The positive symmetric cells used here were cycled to be representative of a 4.5 V UCV in a full cell. Supplementary Fig. 7 shows data for positive symmetric cells cycled to be representative of a 4.3 V UCV; the rates of consumption and production of LiDFOB and LiBF₄ are less than the consumption at 4.5 V, which is analogous to the full cell data shown in Fig. 3d.

To further investigate the mechanisms of electrolyte degradation, single-salt 1.2 M LiDFOB cells were prepared for NMR analysis. Figure 3g shows the salt consumption in the full cells. In this system, which initially contained no LiBF₄ in the electrolyte, LiBF₄ is produced during cycling²⁹ and at a higher rate during cycling at 4.5 V, as shown in the inset. Figure 3h,i shows the single-salt electrolyte degradation in symmetric cells. In the negative symmetric cells, LiDFOB is consumed at approximately the same rate as in the

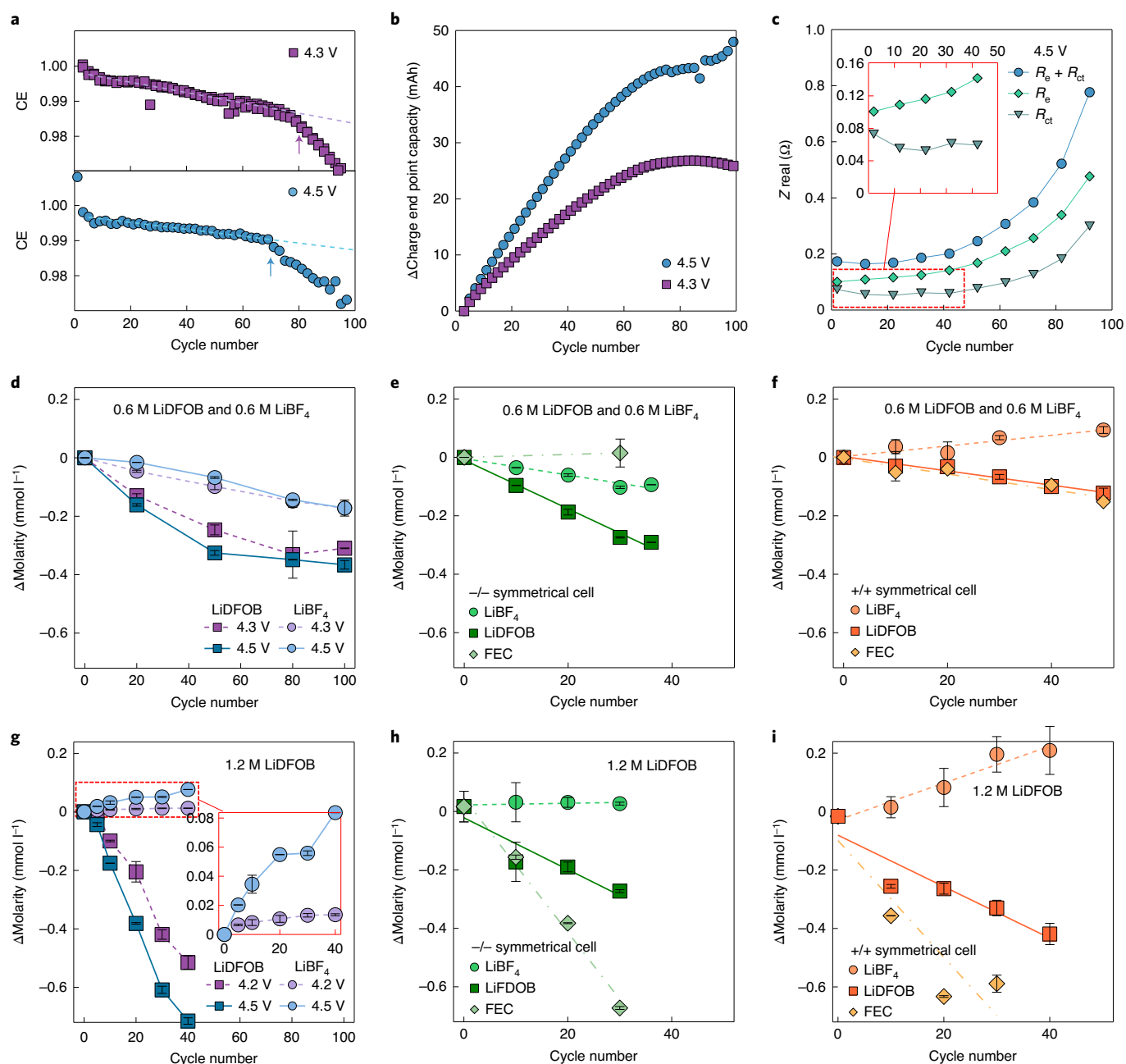


Fig. 3 | Electrochemical and electrolyte analysis. **a,b**, CE (**a**) and zero-charge endpoint capacity (**b**) for dual-salt cells cycled to an UCV of 4.5 V and 4.3 V. **c**, Real components of the impedance (Z_{real}) contributions during 4.5 V cycling; the inset shows a magnified view. **d**, Molarity versus cycle number for dual-salt cells cycled to UCVs of 4.5 V and 4.3 V. **e,f**, Molarity versus cycle number for negative (**e**) and positive (**f**) symmetric dual-salt cells. **g**, Molarity versus cycle number for single-salt cells cycled to UCVs of 4.5 V and 4.2 V; the inset shows a magnified view. **h,i**, Molarity versus cycle number for negative (**h**) and positive (**i**) symmetric single-salt cells. The error bars indicate the range between a pair of measured values, with the data point being the average. The initial salt concentrations are shown at the top of **d-i**. Cycling was performed at 40 °C and under low pressure.

dual-salt negative symmetric cell (Fig. 3e) while the concentration of LiBF_4 remains at zero (Fig. 3h). In the positive symmetric cell, LiDFOB is consumed and LiBF_4 is produced at nearly twice the rate compared to the dual-salt electrolyte cells, suggesting a first-order reaction pathway (Fig. 3i). The electrochemical data for these symmetric cells are shown in Supplementary Fig. 8.

We expect the oxidative decomposition of LiDFOB on the positive electrode in FEC-containing electrolytes to proceed via a LiDFOB ring-opening mechanism, followed by a nucleophilic attack on the FEC carbonyl carbon by a BF_2^- radical (Supplementary Fig. 10a)³³. This oxidative pathway results in the

formation of lithium conducting polymers and oligomer species that passivate the positive electrode and improve cell performance³⁴. Furthermore, the reduction of FEC has been extensively studied^{35–38}, with numerous reports indicating a ring-opening process resulting in the production of one equivalent each of CO_2 and LiF (Supplementary Fig. 10b)^{39–41}. The unreacted LiDFOB undergoes a fluorine–oxygen exchange with the fluorinated boron centre in the polymeric species that results from the decomposition of LiDFOB to produce LiBF_4 (Supplementary Fig. 10c)^{33,42,43}. Finally, the reduction of LiBF_4 is expected to result in the formation of LiF and Li_xBF_y moieties⁴².

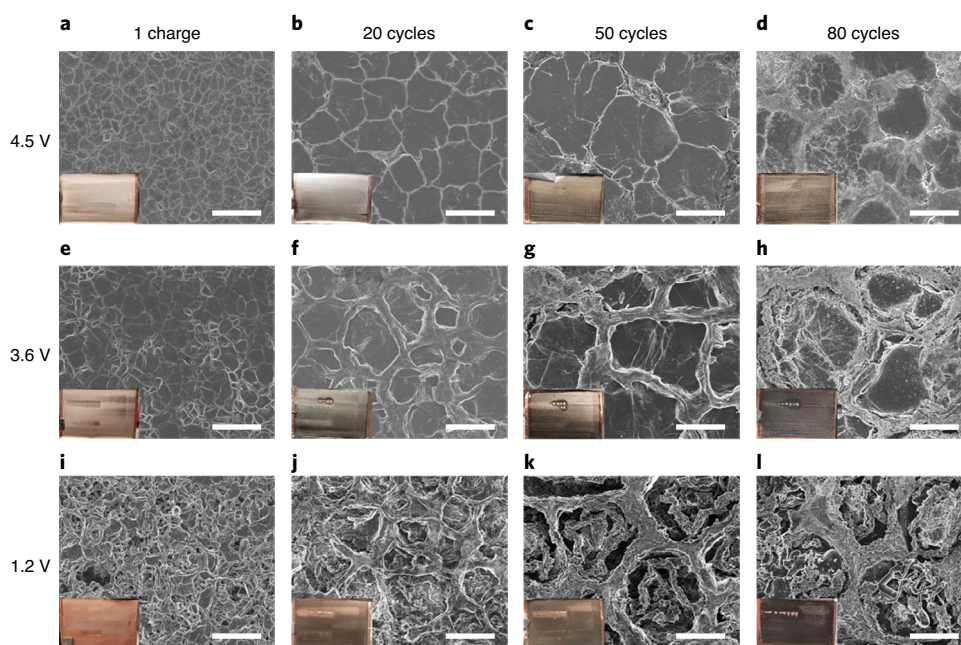


Fig. 4 | Evolution of lithium morphology. **a–l**, SEM images of fully plated lithium (4.5 V, **a–d**), images taken after most of the lithium has been stripped (3.6 V, **e–h**) and images taken after all the active lithium has been stripped (1.2 V, **i–l**) after 1 charge (**a,e,i**), and 20 (**b,f,j**), 50 (**c,g,k**) and 80 (**d,h,l**) cycles. The insets are optical images of lithium plated on a single electrode layer harvested from the pouch cell. The samples were retrieved from cells cycled in a dual-salt electrolyte under high pressure at 40 °C. Scale bars, 25 μm .

These results show that crosstalk plays an important role in the efficacy of the dual-salt electrolyte. Electrolyte oxidation on the positive electrode converts LiDFOB to LiBF_4 , which is beneficial to the lithium electrode. A single-salt, pure LiDFOB electrolyte cycled to low UCVs has no source of LiBF_4 without the occurrence of electrolyte oxidation, which is why it performs worse than a dual-salt electrolyte. However, LiDFOB is also beneficial to the lithium electrode; therefore, its depletion via oxidative decomposition on the positive electrode as well as consumption on the negative electrode precipitates uncontrolled lithium growth and cell failure. Although decomposition of the dual salt is required to stabilize the lithium surface, this failure can be mitigated by operating at a lower UCV to slow the depletion of LiDFOB via oxidative decomposition.

The superior lithium morphology enabled by LiDFOB and LiBF_4 decomposition is likely to result from formation of the SEI. We previously showed that this SEI consists of important LiF and organic fluorine components²⁹. A number of studies have investigated the chemical composition of the SEI to provide speculation of what might be optimal conditions for lithium plating, such as substantial concentrations of LiF (ref. ⁴⁴). However, beyond compositional identification of the SEI that forms in successful cell chemistries, fundamental insight into the engineering of a SEI that facilitates optimal lithium plating has yet to be demonstrated.

Evolution of lithium morphology. Figure 4 shows the evolution of lithium morphology as a function of cycle number for cells cycled under high pressure. The same analysis was performed with cells under low pressure and is shown in Supplementary Fig. 11. To probe the morphology as a function of plating depth, SEM images were taken at three stages of lithium plating: 100% plating at the top of charge (4.5 V, top row); after most of the lithium has been stripped away at the bottom of discharge (3.6 V, middle row); and after all active lithium has been stripped away (1.2 V, bottom row). The insets show optical images of the plated lithium. The lithium appears most pristine in the fully plated state. The dual-salt electrolyte produces an incredibly flat morphology, appearing as a smooth

mosaic composed of tightly packed lithium grains that increase in size throughout the course of 50 cycles (Fig. 4a–c). Such low surface area morphology is ideal for avoiding lithium loss^{11–13}. By 50 cycles (Fig. 4c), mossy lithium deposits begin to appear between the mosaic grains. At 80 cycles (Fig. 4d), the mossy deposits have expanded further between the grains and have begun to fracture. Supplementary Fig. 12 shows energy-dispersive X-ray spectroscopy measurements demonstrating the compositional differences between the smooth lithium grains and the mossy surroundings.

Figure 4e–h shows that, after most of the lithium is stripped (3.6 V), the smooth base of the lithium grains is visible. This indicates that the lithium grains are, in fact, tightly packed lithium columns. Figure 4i–l shows the dead, inactive lithium and SEI components that remain after all of the active lithium is stripped (1.2 V). Figure 4i shows the dead lithium that is generated after a single cycle. After 20 cycles (Fig. 4j), the dead lithium appears patterned; cavities of $\sim 20\mu\text{m}$ are surrounded by walls of dead lithium. It is assumed that the lithium columns are deposited in these cavities, and then push the dead lithium aside to form the mossy walls observed between the smooth lithium grains. This is also observed after 50 and 80 cycles (Fig. 4k–l). Incredibly, the formation of columnar lithium enabled by the dual-salt electrolyte forms a matrix of dead lithium, which facilitates reversible lithium deposition. As the electrolyte degrades with cell ageing, this matrix begins to fill with dead lithium, which hinders the formation of smooth grains as shown in the SEM images obtained after 80 cycles (Fig. 4d). As a result, the loss of capacity accelerates.

Figure 5a–c shows X-ray tomography images of dual-salt cells cycled under high pressure after 1 charge, and 50 and 80 cycles; these cell images were taken at a low state of charge (3.6 V). The electrode stacks are overlaid with a legend to distinguish each component in the stack. Of most interest are the lithium layers that thicken with extended cycling, indicating an increase in lithium porosity. As the porosity increases, the electrolyte within the cell has a larger volume to fill to fully wet all the cell components. As these cells were filled with a lean 0.5 ml volume of electrolyte (2.2 ml Ah^{-1}), insufficient

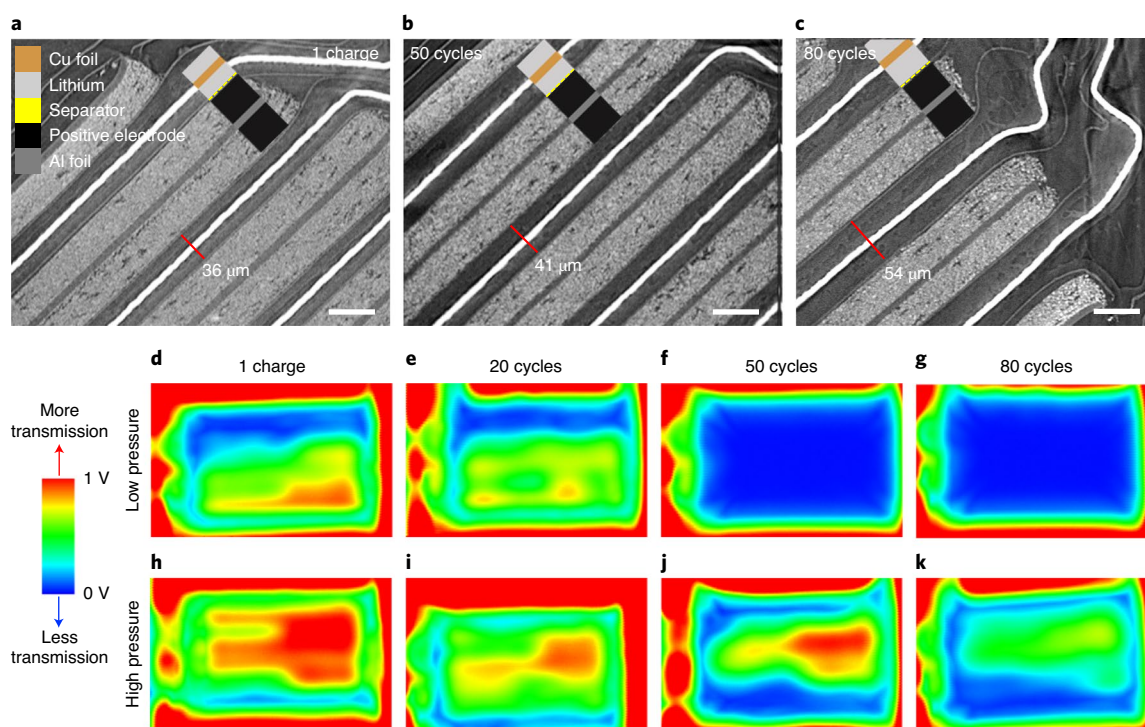


Fig. 5 | The impact of increasing porosity. **a–c**, X-ray tomography images of the anode-free cells after 1 charge (**a**), and 50 (**b**) and 80 (**c**) cycles. Scale bars, 50 μm. **d–k**, Ultrasonic transmission mapping of the anode-free cells constrained under low pressure (**d–g**) and under high pressure (**h–k**) after 1 charge (**d,h**), and 20 (**e,i**), 50 (**f,j**) and 80 (**g,k**) cycles. The cells were cycled with the dual-salt electrolyte at 40 °C.

electrode wetting due to electrolyte dispersion as the porosity increases, referred to as electrolyte depletion, becomes a concern.

To investigate electrolyte depletion, ultrasonic transmission mapping of the dual-salt cells was performed. Previously, other groups have performed acoustic studies of Li-ion pouch cells⁴⁵. Here, we spatially resolved the transmission of an ultrasonic signal through pouch cells as described in the Methods. Cells cycled under low pressure (Fig. 5d–g) and high pressure (Fig. 5h–k) were tested. High-to-low transmission is shown using a red-to-blue heat map. The blue, low transmission, regions indicate insufficient electrode wetting. Supplementary Fig. 13 shows the orientation of the transmission maps relative to a pouch cell. The cells under high pressure exhibit superior electrode wetting as a result of the more compact lithium morphology, as shown in Supplementary Fig. 14. Throughout the extended cycling, electrode wetting deteriorates due to increasing lithium porosity. Under low pressure at 50 cycles (Fig. 5f), there is almost zero transmission, indicating at least one layer of the wound pouch cell is dry⁴⁶. This electrolyte depletion also contributes to the increasing value of R_c shown in Fig. 3c.

Safety characterization. Figure 6 shows the results of two safety characterization tests. First, we qualitatively examined lithium reactivity by submerging plated lithium in water (Fig. 6b–e). For reference, we also submerged a sample of charged graphite (Fig. 6a), which produced a large amount of gas and foamed when submerged in water. Figure 6b,c shows the plated lithium samples produced with the dual-salt electrolyte after 20 and 80 cycles, respectively. The 20-cycle sample of pristine lithium merely gassed and foamed, similar to the graphite sample, while the 80-cycle sample produced a small flame. Figure 6d,e shows the lithium samples produced with 1.2M LiPF₆ in FEC:DEC and EC:DEC electrolytes, respectively. These primitive electrolytes produced highly mossy lithium samples and caused large explosions when submerged in water. Figure 6b–e qualitatively

shows that lithium with a pristine morphology exhibits mild reactivity, analogous to charged graphite, when submerged in water.

Figure 6f–k shows the results of ‘smart’ nail tests performed on anode-free pouch cells cycled under low pressure. This smart nail has a thermocouple attached to the nail tip, allowing the temperature to be measured at the point of penetration⁴⁷. The cells were penetrated at the top of charge (4.5 V) after 1 charge, and 20 and 50 cycles. Figure 6i–k shows the temperature versus time for cells with the dual-salt electrolyte, cells with 1.73 M LiFSI dimethoxyethane (DME):1,1,2,2-tetrafluoroethyl-2,2,3,3-tetrafluoropropyl ether (TTE) electrolyte reported in the literature¹⁸ and with a 4 M LiFSI FEC:DEC electrolyte. Figure 6f–h shows images taken during nail tests of cells with these electrolytes after 50 cycles. The peak temperature of the cells with dual-salt electrolyte increased throughout 50 cycles but never exceeded 100 °C; furthermore, these cells did not explode. The peak temperature of the cells with 1.73 M LiFSI DME:TTE and 4 M LiFSI FEC:DEC electrolytes increased throughout 20 cycles, then, after 50 cycles, both of these chemistries resulted in violent explosions, reaching maximum temperatures of 500 °C and 370 °C, respectively. Videos of these nail tests are available as Supplementary Information. It is clear that cells with the dual-salt electrolyte are considerably safer than the other chemistries tested in this study.

High-concentration dual-salt electrolyte. This study has shown that the dual-salt electrolyte enables pristine lithium morphology at the expense of LiDFOB and LiBF₄ consumption. Therefore, optimization of salt concentration is an obvious way to increase the lifetime of the cells. Increasing the volume of electrolyte would analogously increase the lifetime as shown in Supplementary Fig. 15; however, here we wanted to retain the use of a lean 2.2 ml Ah^{−1} electrolyte to maximize energy density. Figure 7 shows the cycling performance for cells made with a high-concentration dual-salt electrolyte, 2 M LiDFOB and 1.4 M LiBF₄. In addition to cycling

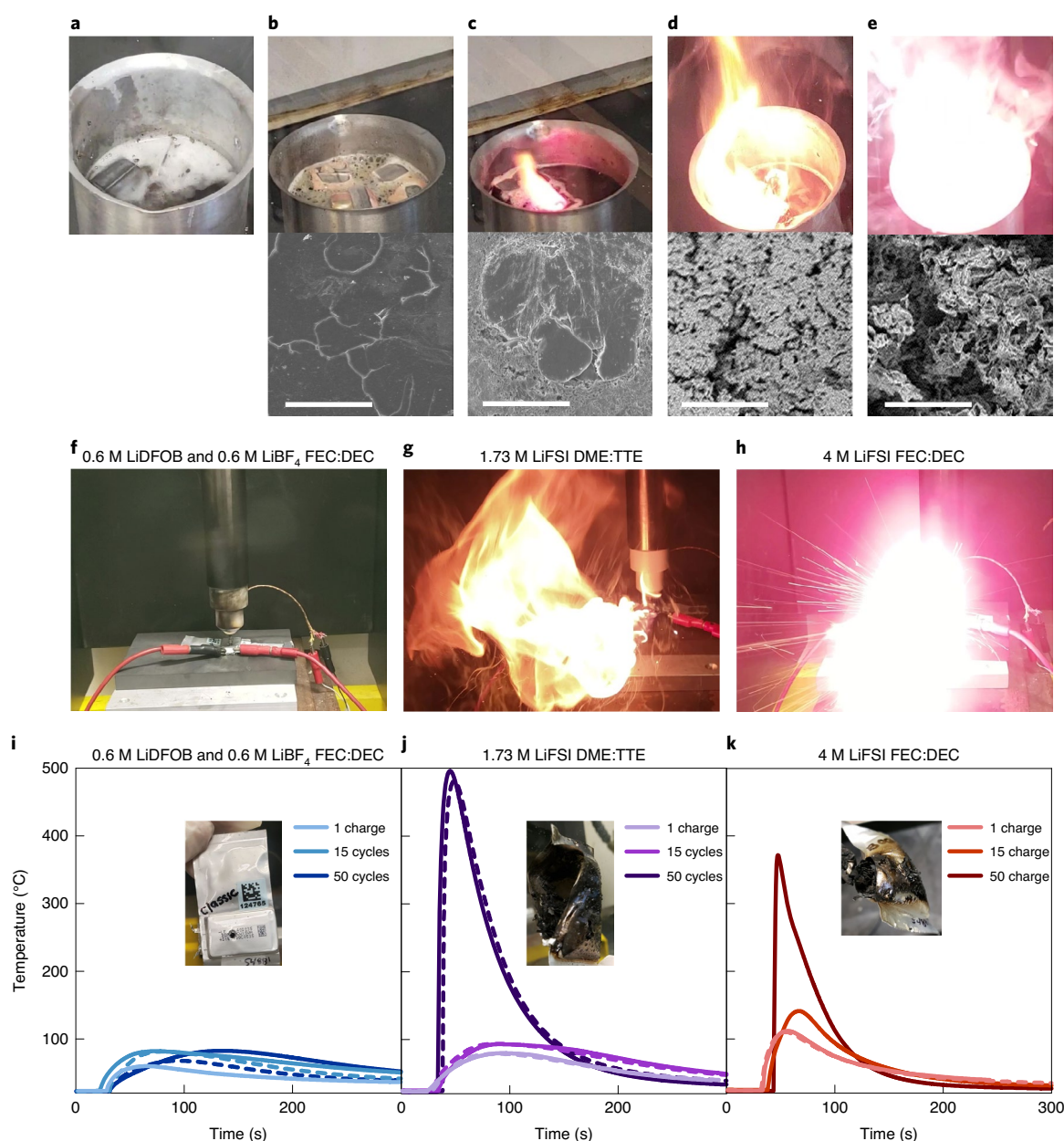


Fig. 6 | Safety characterization. **a**, Charged graphite submerged in water. **b–e**, Plated lithium samples submerged in water (top) and the respective lithium morphology of the submerged samples (bottom). The lithium samples were produced using dual-salt electrolyte (**b,c**), 1.2 M LiPF₆ in FEC:DEC (**d**) and EC:DEC (**e**) electrolytes. The graphite and lithium samples were retrieved from fully charged cells. Scale bars, 25 μ m. **f–h**, The anode-free cells undergoing nail penetration after 50 cycles. **i–k**, Temperature versus time of the cells during nail penetration and images of the anode-free cells after 50 cycles following nail penetration (insets). The nail tests were performed on cells in a fully charged state. The electrolytes used for cells in the nail test were dual-salt electrolyte (**f,i**), 1.73 M LiFSI DME:TTE (**g,j**) and 4 M LiFSI FEC:DEC (**h,k**).

at 40 °C, we also demonstrate the performance at 20 °C enabled by a 40 °C hot-formation protocol described previously⁴⁸. Figure 7a shows the normalized capacity versus cycle number. The high-concentration dual-salt cells outperform the 0.6 M LiDFOB and 0.6 M LiBF₄ mixture, with cells cycled under high pressure at 20 °C sustaining the longest lifetime of 200 cycles to 80% capacity. Also of note is the performance of the high-concentration dual-salt cells tested under low pressure, enabling competitive performance in comparison with the normal dual-salt cells constrained to high pressure. However, the most practical performance metric is energy retention over Li-ion cells. Figure 7b shows energy density versus cycle number for the high-concentration dual-salt cells

compared to Li-ion cells. The cells cycled at 20 °C have a lower initial energy because of worse kinetics at lower temperatures. Figure 7b shows that the high-concentration dual-salt cells cycled under high pressure sustain an energy density higher than an optimized Li-ion chemistry for 200 cycles. Figure 7c,d shows SEM images of the lithium morphology of a sample taken from a cell cycled under high pressure at 40 °C after 100 cycles. The images are from two different locations on the sample, which is shown in the inset of Fig. 7d. Comparing these images to the morphology evolution exhibited in Fig. 4 demonstrates that high-concentration dual-salt electrolytes enable a longer-lasting pristine lithium morphology, thus improving lifetime.

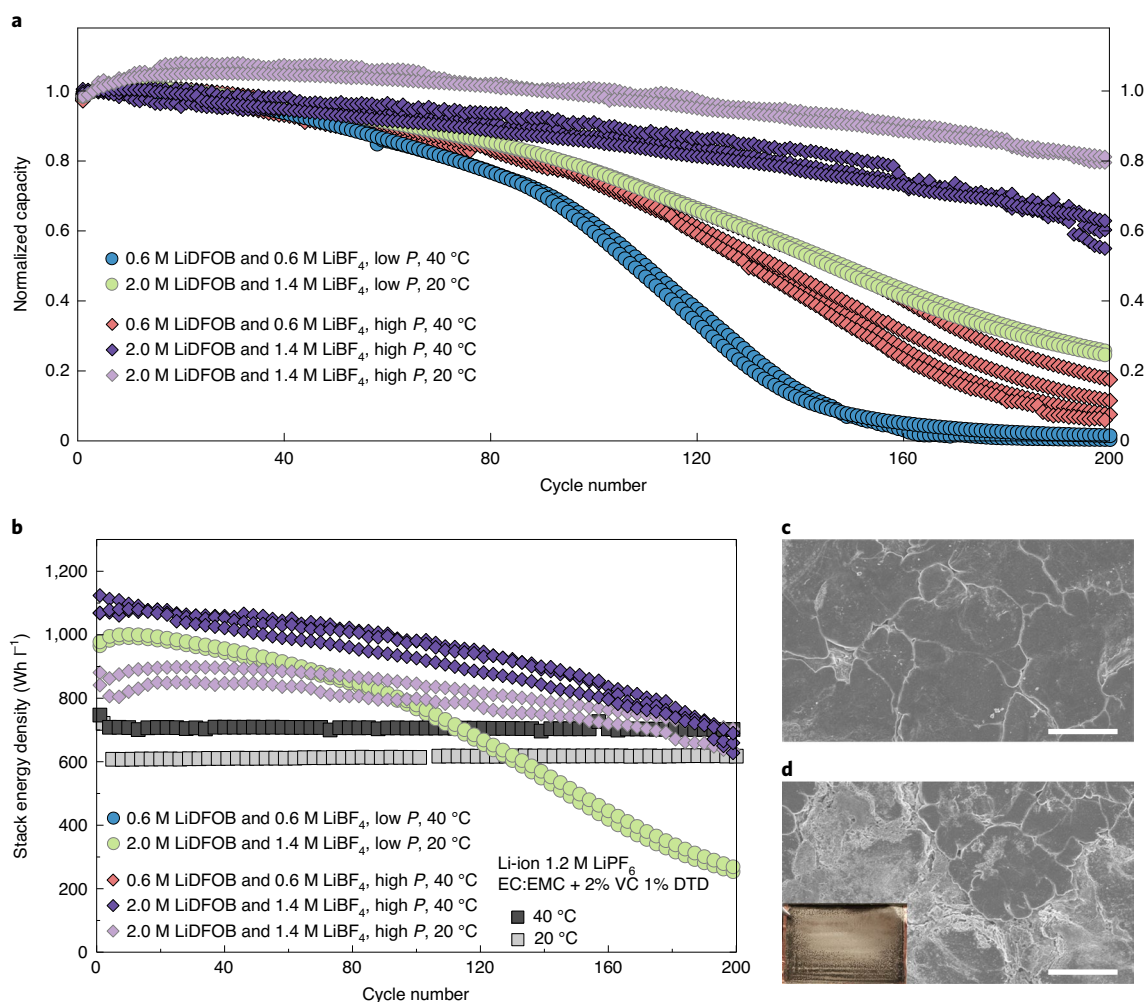


Fig. 7 | High-concentration dual-salt electrolyte. **a**, Normalized capacity versus cycle number. **b**, Stack energy density versus cycle number. **c, d**, SEM images of the lithium morphology after 100 cycles for cells with a 2 M LiDFOB and 1.4 M LiBF₄ electrolyte cycled under high pressure at 40 °C taken from two different areas on the electrode shown in the inset; the inset is an optical image of lithium plated on a single electrode layer harvested from the pouch cell. Scale bars, 25 μ m.

Conclusions

A dual-salt LiDFOB and LiBF₄ electrolyte has been demonstrated to extend the lifetime of anode-free cells to 200 cycles. This synergistic salt combination enables pristine lithium deposition and formation of a smooth mosaic of tightly packed lithium columns. We have shown that lithium-electrolyte reactions involving the consumption of both LiDFOB and LiBF₄ enable this highly favourable lithium morphology. As a result, the electrolyte is eventually exhausted of these salt components and the lithium morphology begins to degrade. As the porosity of the lithium electrode increases concomitant with salt exhaustion, the electrolyte must fill a larger volume that eventually results in electrolyte depletion and impedance growth. These factors contribute to capacity loss and death of the anode-free cells. We have shown that, when the cells are constrained under higher pressures, their lifetime is extended by maintaining a lower surface area and less porous morphology, thereby delaying these degradation mechanisms.

This work represents the state-of-the-art for the highest energy density anode-free lithium metal cells with the longest lifetime. Moreover, we have demonstrated that these cells may have reached an acceptable safety standard without the use of a solid-state electrolyte. Nevertheless, increased lifetime is required before such cells will be viable for electric vehicles or electrified

urban aviation. If further progress in lifetime can be achieved, anode-free lithium metal cells with liquid electrolytes present the most straightforward and low-cost path towards viable high energy density lithium batteries.

Methods

Electrochemical testing. Wound, 230 mAh pouch cells were received dry from Li-FUN Technology (Xinma Industry Zone). The positive electrode was a single-crystal LiNi_{0.5}Mn_{0.3}Co_{0.2}O₂ (NMC532) material⁴⁹ with an areal capacity of 3.1 mAh cm⁻² and the negative electrode was a bare copper foil. The first charge–discharge voltage versus capacity curves for these anode-free pouch cells are shown in Supplementary Fig. 16. The dimensions of each component of the cell stack are listed in Supplementary Table 1. The cells were filled with 0.5 ml (~2.6 g Ah⁻¹, 2.2 ml Ah⁻¹) of electrolyte in an argon glovebox. The dual-salt electrolyte contained 0.6 M LiDFOB (Capchem, 99%) and 0.6 M LiBF₄ (BASF, 99%) in FEC (Capchem, 99.4%) and DEC (Capchem, >99%) in a ratio of 1:2 v:v. The cycle testing was performed on a MACCOR Series 4000 charger at charge and discharge current densities of 0.58 mA cm⁻² and 1.44 mA cm⁻², respectively, corresponding to C/5 and D/2 current rates between 3.6 and 4.5 V. The CE and charge endpoint capacity measurements were performed on a Novonix ultra high precision charger. Testing was performed at 40 °C and 20 °C (± 0.1 °C) in temperature boxes.

Stack energy density calculations. To calculate the stack energy density, first the areal loading was determined by dividing the discharge capacity by the total positive electrode area of 86.58 cm². One stack is considered to be a sandwich composed of a double-sided positive electrode, a separator, a double-sided negative electrode and another separator. As the stack contains two pairs of electrodes,

the areal loading was multiplied by two, and was then divided by the total stack thickness or stack mass per unit area (given in Supplementary Table 1) and converted to the correct units to determine the Wh l^{-1} and Wh kg^{-1} . The positive electrode, current collectors and separator thickness and mass values are listed in Supplementary Table 1. The graphite negative electrode values for the Li-ion cell are also listed in Supplementary Table 1. The lithium electrode thickness for the anode-free cells was determined to be $\sim 15.5 \mu\text{m}$ using the capacity plated during the first charge. It should be noted that this calculation does not account for swelling of the lithium electrode, which is known to occur during cycling.

SEM imaging. After cycling, the pouch cells were opened in an argon-filled glovebox. The lithium electrodes were unwound, punched into $\sim 0.5 \text{ cm}^2$ samples and washed with dimethyl carbonate. The samples were transported from the glovebox to a Hitachi S-4700 field emission scanning electron microscope in an airtight container. The samples were briefly ($< 10 \text{ s}$) exposed to air while they were loaded in the SEM. The SEM images were taken in secondary electron imaging mode with an accelerating voltage of 3.0 kV and a working distance of 12 mm .

X-ray tomography imaging. X-ray tomographic imaging was performed using a Zeiss Xradia Versa 520 X-ray microscope (XRM) (Carl Zeiss X-ray Microscopy Inc.). The unique architecture of the XRM allows non-destructive visualization and high-resolution imaging of the internal morphology of the anode-free pouch cell. All imaging was performed without opening or otherwise disturbing the packaging. The XRM employs a tungsten target anode with potential accelerating voltage range from 30 to 160 kV . Here, an accelerating voltage of 80 kV was used in addition to the (proprietary) LE1 source filter. During the tomography, $1,601$ projection images were acquired over an angle range from -183° to 3° utilizing the $\times 4$ optical magnification objective. This resulted in a pixel size of $0.7 \mu\text{m}$. Reconstruction was performed using a commercial software package, XMReconstructor (Carl Zeiss X-ray Microscopy Inc.), utilizing a cone-beam filtered back-projection algorithm.

NMR electrolyte analysis. For electrolyte extraction, the pouch cells were cut open in a glovebox and filled with 1 ml of anhydrous deuterated dimethylsulfoxide (d-DMSO). The solvent was allowed to mix into the jelly roll for 5 min . The symmetric coin cells were opened in a glovebox and the electrodes were placed in a PTFE vial with 1 ml of d-DMSO and shaken for approximately 5 min . The electrolyte-DMSO mixture was then extracted and analysed using liquid NMR on a Bruker AV500 spectrometer.

Ultrasonic transmission mapping. Ultrasonic transmission mapping was performed using an ultrasonic battery scanner (UBSC-LD50, Jiangsu Jitri-Hust Intelligent Equipment Technology Co., Ltd)⁴⁶. A pair of ultrasonic focus transducers (2 MHz frequency, 30 mm focal distance, customized from Shantou Institute of Ultrasonic Instruments Co., Ltd.) were positioned on either side of the cell. The transducers and cells were immersed in low-viscosity silicone oil that serves as an ultrasonic coupling agent. The transducers were installed on a two-dimensional motion system with a precision of 0.2 mm to perform mechanical progressive scanning. The ultrasonic signal was emitted by a transducer on one side of the cell and received by the transducer on the other side. The driving source was a 200-V pulse signal with a pulse width of 250 ns , which matches the 2-MHz ultrasonic transducer used in this study. The waveform of the transmitted signal was recorded with a collecting card. The peak-to-peak values of the received transmission waves were converted into colour heat maps to produce the pseudo-colour images. The cells were degassed before the ultrasonic measurements, which were performed at 20°C .

Smart nail safety characterization. The cells were charged to 4.5 V with a 1-h hold at the top of charge before nail testing. The smart nails were used to perform the penetration. The shafts of these nails were hollow so that a thermocouple could be threaded through and attached to the copper tip, as described previously⁴⁷. The nail was driven in to the pouch cells at a rate of $0.52 \pm 0.1 \text{ cm s}^{-1}$ with an Enerpac A258 hydraulic press connected to an Enerpac PER1301B hydraulic pump.

Data availability

All relevant data are included in the paper and its Supplementary Information. Source data are provided with this paper.

Received: 4 April 2020; Accepted: 6 July 2020;

Published online: 10 August 2020

References

- Kasliwal, A. et al. Role of flying cars in sustainable mobility. *Nat. Commun.* **10**, 1555 (2019).
- Holden, J. & Goel, N. *Fast-forwarding to a Future of On-demand Urban Air Transportation* (Uber Elevate, 2016); <https://www.uber.com/elevate.pdf>
- Blomgren, G. E. The development and future of lithium ion batteries. *J. Electrochem. Soc.* **164**, A5019–A5025 (2017).
- Neudecker, B. J., Dudney, N. J. & Bates, J. B. 'Lithium-free' thin-film battery with in situ plated Li anode. *J. Electrochem. Soc.* **147**, 517 (2000).
- Qian, J. et al. Anode-free rechargeable lithium metal batteries. *Adv. Funct. Mater.* **26**, 7094–7102 (2016).
- Albertus, P., Babinec, S., Litzelman, S. & Newman, A. Status and challenges in enabling the lithium metal electrode for high-energy and low-cost rechargeable batteries. *Nat. Energy* **3**, 16–21 (2018).
- Liu, J. et al. Pathways for practical high-energy long-cycling lithium metal batteries. *Nat. Energy* **4**, 180–186 (2019).
- Schmuck, R., Wagner, R., Hörpel, G., Placke, T. & Winter, M. Performance and cost of materials for lithium-based rechargeable automotive batteries. *Nat. Energy* **3**, 267–278 (2018).
- Betz, J. et al. Theoretical versus practical energy: a plea for more transparency in the energy calculation of different rechargeable battery systems. *Adv. Energy Mater.* **9**, 1803170 (2018).
- Abrha, L. H. et al. $\text{Li}_2\text{La}_{2.75}\text{Ca}_{0.25}\text{Zr}_{1.75}\text{Nb}_{0.25}\text{O}_{12}/\text{LiClO}_4$ composite film derived solid electrolyte interphase for anode-free lithium metal battery. *Electrochim. Acta* **325**, 134825 (2019).
- Aurbach, D., Zinigrad, E., Cohen, Y. & Teller, H. A short review of failure mechanisms of lithium metal and lithiated graphite anodes in liquid electrolyte solutions. *Solid State Ion.* **148**, 405–416 (2002).
- Lin, D., Liu, Y. & Cui, Y. Revisiting the lithium metal anode for high-energy batteries. *Nat. Nanotechnol.* **12**, 194–206 (2017).
- Fang, C. et al. Quantifying inactive lithium in lithium metal batteries. *Nature* **572**, 511–515 (2019).
- Ding, F. et al. Effects of carbonate solvents and lithium salts on morphology and Coulombic efficiency of lithium electrode. *J. Electrochem. Soc.* **160**, A1894–A1901 (2013).
- Wood, K. N. et al. Dendrites and pits: untangling the complex behavior of lithium metal anodes through operando video microscopy. *ACS Cent. Sci.* **2**, 790–801 (2016).
- López, C. M., Vaughey, J. T. & Dees, D. W. Morphological transitions on lithium metal anodes. *J. Electrochem. Soc.* **156**, A726 (2009).
- Rodríguez, R. et al. Separator-free and concentrated LiNO_3 electrolyte cells enable uniform lithium electrodeposition. *J. Mater. Chem. A* <https://doi.org/10.1039/c9ta10929c> (2020).
- Ren, X. et al. Enabling high-voltage lithium-metal batteries under practical conditions. *Joule* **3**, 1662–1676 (2019).
- Chen, S. et al. High-voltage lithium-metal batteries enabled by localized high-concentration electrolytes. *Adv. Mater.* **30**, 1–7 (2018).
- Wilkinson, D. P., Blom, H., Brandt, K. & Wainwright, D. Effects of physical constraints on Li cyclability. *J. Power Sources* **36**, 517–527 (1991).
- Louli, A. J. et al. Exploring the impact of mechanical pressure on the performance of anode-free lithium metal cells. *J. Electrochem. Soc.* **166**, A1291–A1299 (2019).
- Yin, X. et al. Insights into morphological evolution and cycling behaviour of lithium metal anode under mechanical pressure. *Nano Energy* **50**, 659–664 (2018).
- Niu, C. et al. High-energy lithium metal pouch cells with limited anode swelling and long stable cycles. *Nat. Energy* **4**, 551–559 (2019).
- Brandt, K. Historical development of secondary lithium batteries. *Solid State Ion.* **69**, 173–183 (1994).
- Zhang, H. et al. Ionic liquid electrolyte with highly concentrated LiTFSI for lithium metal batteries. *Electrochim. Acta* **285**, 78–85 (2018).
- Guo, Q. et al. Flame retardant and stable $\text{Li}_{1.5}\text{Al}_{0.5}\text{Ge}_{1.5}(\text{PO}_4)_3$ -supported ionic liquid gel polymer electrolytes for high safety rechargeable solid-state lithium metal batteries. *J. Phys. Chem. C* **122**, 10334–10342 (2018).
- von Saken, U., Nodwell, E., Sundher, A. & Dahn, J. R. Comparative thermal stability of carbon intercalation anodes and lithium metal anodes for rechargeable lithium batteries. *J. Power Sources* **54**, 240–245 (1995).
- Zhou, Q. et al. A temperature-responsive electrolyte endowing superior safety characteristic of lithium metal batteries. *Adv. Energy Mater.* **10**, 1–8 (2020).
- Weber, R. et al. Long cycle life and dendrite-free lithium morphology in anode-free lithium pouch cells enabled by a dual-salt liquid electrolyte. *Nat. Energy* **4**, 683–689 (2019).
- Smith, A. J., Burns, J. C., Xiong, D. & Dahn, J. R. Interpreting high precision coulometry results on Li-ion cells. *J. Electrochem. Soc.* **158**, A1136–A1142 (2011).
- Nelson, K. J. et al. Studies of the effect of high voltage on the impedance and cycling performance of $\text{Li}[\text{Ni}_{0.4}\text{Mn}_{0.4}\text{Co}_{0.2}]\text{O}_2$ /graphite lithium-ion pouch cells. *J. Electrochem. Soc.* **162**, A1046–A1054 (2015).
- Nelson, K. *Studies of the Effects of High Voltage on the Performance and Impedance of Lithium-ion Batteries*. PhD thesis, Dalhousie Univ. (2017).
- Zhu, Y., Li, Y., Bettge, M. & Abraham, D. P. Positive electrode passivation by LiDFOB electrolyte additive in high-capacity lithium-ion cells. *J. Electrochem. Soc.* **159**, A2109–A2117 (2012).
- Cha, J., Han, J. G., Hwang, J., Cho, J. & Choi, N. S. Mechanisms for electrochemical performance enhancement by the salt-type electrolyte additive, lithium difluoro(oxalato)borate, in high-voltage lithium-ion batteries. *J. Power Sources* **357**, 97–106 (2017).

35. Chen, X. et al. Reduction mechanism of fluoroethylene carbonate for stable solid-electrolyte interphase film on silicon anode. *ChemSusChem* **7**, 549–554 (2014).
36. Streich, D. et al. Online electrochemical mass spectrometry of high energy lithium nickel cobalt manganese oxide/graphite half- and full-cells with ethylene carbonate and fluoroethylene carbonate based electrolytes. *J. Electrochem. Soc.* **163**, A964–A970 (2016).
37. Nakai, H., Kubota, T., Kita, A. & Kawashima, A. Investigation of the solid electrolyte interphase formed by fluoroethylene carbonate on Si electrodes. *J. Electrochem. Soc.* **158**, A798 (2011).
38. Schroder, K. et al. The effect of fluoroethylene carbonate as an additive on the solid electrolyte interphase on silicon lithium-ion electrodes. *Chem. Mater.* **27**, 5531–5542 (2015).
39. Jung, R. et al. Consumption of fluoroethylene carbonate (FEC) on Si-C composite electrodes for Li-ion batteries. *J. Electrochem. Soc.* **163**, A1705–A1716 (2016).
40. Petibon, R. et al. Studies of the capacity fade mechanisms of LiCoO_2/Si -alloy:graphite cells. *J. Electrochem. Soc.* **163**, A1146–A1156 (2016).
41. Xu, C. et al. Improved performance of the silicon anode for Li-ion batteries: understanding the surface modification mechanism of fluoroethylene carbonate as an effective electrolyte additive. *Chem. Mater.* **27**, 2591–2599 (2015).
42. Parimalam, B. S. & Lucht, B. L. Reduction reactions of electrolyte salts for lithium ion batteries: LiPF_6 , LiBF_4 , LiDFOB , LiBOB , and LiTFSI . *J. Electrochem. Soc.* **165**, A251–A255 (2018).
43. Allen, J. L., Han, S. D., Boyle, P. D. & Henderson, W. A. Crystal structure and physical properties of lithium difluoro(oxalato) borate (LiDFOB or LiBF_2O_x). *J. Power Sources* **196**, 9737–9742 (2011).
44. Jurng, S., Brown, Z. L., Kim, J. & Lucht, B. L. Effect of electrolyte on the nanostructure of the solid electrolyte interphase (SEI) and performance of lithium metal anodes. *Energy Environ. Sci.* <https://doi.org/10.1039/C8EE00364E> (2018).
45. Bommier, C. et al. In operando acoustic detection of lithium metal plating in commercial $\text{LiCoO}_2/\text{Graphite}$ pouch cells. *Cell Rep. Phys. Sci.* <https://doi.org/10.1016/j.xcrp.2020.100035> (2020).
46. Deng, Z. et al. Observation of the electrolyte wetting and ‘unwetting’ in Li-ion pouch cells via ultrasonic scanning technology. *Joule* <https://doi.org/10.1016/j.joule.2020.07.014> (2020).
47. Hatchard, T. D., Trussler, S. & Dahn, J. R. Building a ‘smart nail’ for penetration tests on Li-ion cells. *J. Power Sources* **247**, 821–823 (2014).
48. Genovese, M. et al. Hot formation for improved low temperature cycling of anode-free lithium metal batteries. *J. Electrochem. Soc.* **166**, A3342–A3347 (2019).
49. Li, J. et al. Comparison of single crystal and polycrystalline $\text{LiNi}_{0.5}\text{Mn}_{0.3}\text{Co}_{0.2}\text{O}_2$ positive electrode materials for high voltage Li-ion cells. *J. Electrochem. Soc.* **164**, A1534–A1544 (2017).

Acknowledgements

This research was financially supported by Tesla Canada and NSERC under the Industrial Research Chairs Program. A.J.L. and A.E. thank NSERC, the Killam Foundation and the Nova Scotia Graduate Scholarship programmes for financial support. M.G. thanks the NSERC PDF Program. We acknowledge J. Li (formerly of BASF) and D. J. Xiong (formerly of Capchem) for providing the chemicals used in the electrolytes. We also acknowledge P. Scallion for SEM support, as well as S. Trussler for expert fabrication of the parts used in this work.

Author contributions

A.J.L., M.G., R.W. and J.R.D. conceived the idea. A.J.L. performed the electrochemical measurements and the SEM analysis with the assistance of M.C. and J.d.G. A.E. and R.W. performed and analysed the NMR experiments with the assistance of M.C. and J.d.G. X-ray tomography was performed by R.T.W., J.L. and T.R. A.J.L. performed the safety characterization with the assistance of J.d.G. Z.D. performed the ultrasonic transmission mapping measurements. R.P., S.J.H.C. and S.H. contributed to useful discussions. A.J.L., A.E. and J.R.D. prepared the manuscript with input from all other co-authors.

Competing interests

R.W., R.P., S.H. and S.J.H.C. are employed by Tesla Canada R&D. R.T.W., J.L. and T.R. are employed by Carl Zeiss Microscopy.

Additional information

Supplementary information is available for this paper at <https://doi.org/10.1038/s41560-020-0668-8>.

Correspondence and requests for materials should be addressed to J.R.D.

Reprints and permissions information is available at www.nature.com/reprints.

Publisher's note Springer Nature remains neutral with regard to jurisdictional claims in published maps and institutional affiliations.

© The Author(s), under exclusive licence to Springer Nature Limited 2020